Influence of Near-blade hydrodynamics on Cross-flow Turbine performance

Abigale Snortland, Brian Polagye, and Owen Williams

Abstract— **Phase-averaged 2D planar PIV data for an optimal and sub-optimal tip-speed ratio ($\lambda = 1.1$ and 1.9, respectively) is captured over the upstream and downstream sweep of two-bladed, straight bladed cross-flow turbine. The azimuthally varying near-blade hydrodynamics are examined in concert with phase-averaged performance data. Both the near-blade and near-wake hydrodynamics are shown to be highly dependent on tip speed ratio and azimuthal position and the implications on power production are discussed. The flow field surrounding downstream blades appears to be critical to overall turbine performance, with strong and persistent stall and vortex interactions appearing to lead to downstream blade forces that exceed increases in lift on the upstream blade due to a strong leading-edge vortex at $\lambda = 1.1$. Upstream blade vortex shedding is significantly delayed for $\lambda = 1.9$. This, combined with a weakly stalled downstream blade, yields a significant increase in turbine performance. Differences between flow patterns observed in this and previous studies suggest an influence of Reynolds number.**

Keywords— **Particle Image Velocimetry, Cross-Flow Turbine, Near-blade Hydrodynamics, Dynamic Stall, Vortex Dynamics**

I. INTRODUCTION

CROSS-FLOW turbines are a promising technology for harvesting the kinetic energy from tides and rivers. While they appear deceptively simple due to fixed blades and lower operational speeds than their axial flow counterparts, the blades experience strong changes in angle of attack, leading to dynamic stall, vortex shedding, and complex interactions between blade wake patterns. Such phenomena have an important impact on power generation, efficiency, and forces on the turbine that are not yet well-understood. A robust understanding of local flow features in the vicinity of the turbine blades and their impact on phase averaged performance is essential for improving power extraction and efficiency and can inform control strategy development and turbine array design.

Dynamic stall of the turbine blades has been shown to

be critical to their performance and is caused by strong variations in blade angle of attack throughout a rotation. The fast variation in angle of attack leads to the roll up a strong suction-side vortex that allows the stall angle to increase much beyond its static angle, increasing lift. Eventually this leading-edge vortex (LEV) detaches and is convected downstream, leading to a considerable drop in blade performance as it leaves the trailing edge [1]. This vortex may also interact with a trailing-edge vortex (TEV). The longer the LEV remains attached during a blade rotation, the higher the dynamic stall angle, and the greater the lift generation, resulting in better turbine performance [2]. Because vortex formation and separation are strongly affected by boundary layer dynamics, these phenomena also depend on the Reynold's number. For example, at higher Reynolds number, separation is delayed until higher angles of attack [3].

The flow dynamics around the downstream blade significantly differ from those of the upstream blade. As the blade moves from the upstream to the downstream side, the angle of attack becomes positive and the suction side flips to the outside of the blade. The downstream blade also operates in a region of much lower velocity due the momentum drop across the turbine rotor and has the potential to interact with any previously shed vortices. For this reason, it is important to study the flow for both the upstream and downstream regions.

Study of dynamic stall and cross-flow turbine blade-wake interactions has received considerable computational and experimental attention. Near-blade hydrodynamics and performance for cross-flow turbines are highly dependent the non-dimensional tip speed ratio, defined as $\lambda = r\omega/U_\infty$. It is the ratio of the turbine blade tangential velocity ($r\omega$) and the freestream (U_∞), where r is the turbine radius to the quarter chord and ω is the rotational velocity of the turbine. Several groups have used planar particle image velocimetry (PIV) [4-7] to capture the near-blade hydrodynamics inside cross-flow turbine rotors. Simão et al. [4] and Fujisawa and Shibuya [5] have
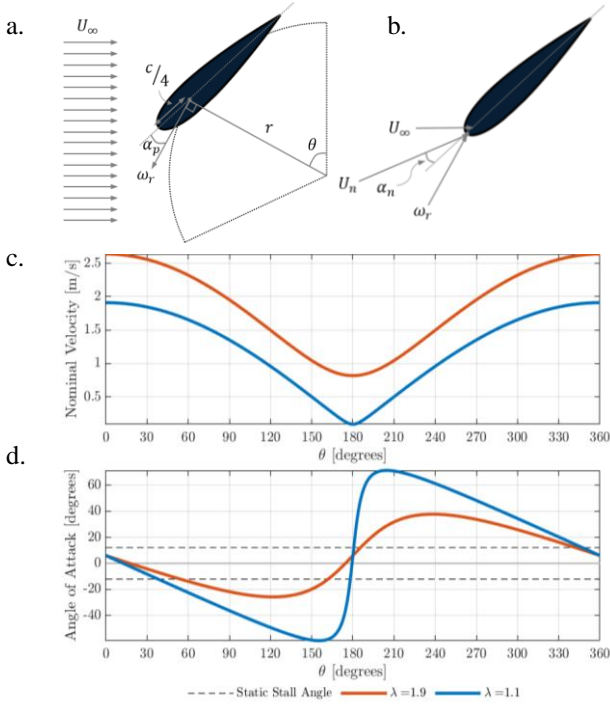
Fig. 1. Schematic of turbine definitions (a,b), nominal velocity (c) and nominal angle of attack (d) for a NACA-0018 Foil for λ=1.9 and 1.1. The static stall angle (12.1°) [9] is plotted for reference at a similar Reynold's number of Re_c=1.5x10⁵.

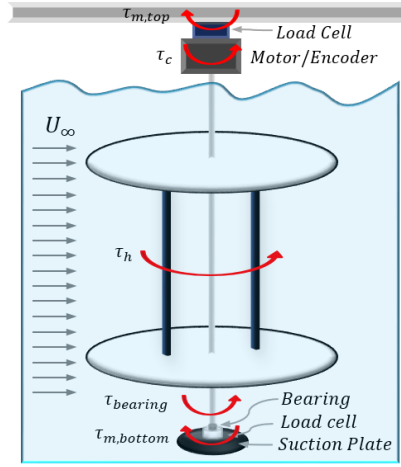Fig. 2. Experimental setup and free body diagram for the experimental setup. The applied torques are τ_h, τ_c, $\tau_{bearing}$ and the measured torques are $\tau_{m,top}$ and $\tau_{m,bottom}$.

demonstrated that the size, strength, and convection speed of the shed vortices depend on λ. Jonathan et al. [6] coupled similar findings with time-averaged performance data. They concluded that a combination of delayed stall and earlier flow re-attachment lead to an increase performance. Somoano and Huera-Huarte [7] also looked at time-averaged performance data and found that for lower λ there is strong interaction between the downstream blade and vortices shed from the upstream blade. They also noted that the local tangential velocity component is high for tip speeds with good performance, and that little lift is produced and the flow is dominated by the rotation for relatively high tip speeds (e.g., a turbine approaching a freewheel condition).

Despite the contributions of these previous studies, flow features have yet to be directly compared to phase-averaged performance characteristics. Such information is critical for our understanding of locally high or low performance phases throughout the rotational cycle. For example, [8] phase averaged power coefficients greater than unity have been observed for some cross-flow turbines operating at tip-speed ratios corresponding with maximum efficiency, which implies greater energy extraction at these phases than is available in the flow. Similarly, it has been shown that the phases of maximum and minimum power extraction vary with tip-speed ratio and so it is difficult to link specific flow field features to turbine performance. Finally, even though the effect of Reynolds number on dynamic stall is well-established, previous studies have explored turbine dynamics at relatively low Reynolds numbers (Re <2x10⁴ based on the blade chord and inflow velocity).

Here, we conduct a series of experiments to explore the near-blade hydrodynamics of cross-flow turbines, linking phase-averaged particle image velocimetry (PIV) flow field measurements to phase-averaged performance characteristics at Reynolds number in terms of the blade chord and turbine diameter of 4.5x10⁴ and 1.9x10⁵, respectively. Blade hydrodynamics are examined for phases of maximum and minimum power extraction for tip-speed ratios with close-to-optimal and poor performance, λ=1.9 and 1.1 respectively. Images are taken for upstream and downstream phases in order to capture the entire blade rotation and any secondary interactions between shed vortices and the blades as they travel downstream.

II. EXPERIMENTAL METHODS

A. Flume

Experiments were run in a 75 cm wide flume with a mean dynamic depth of 56 cm. The fluid was water at 29°C with a density (ρ) of 996 kg/m³ and a dynamic viscosity (μ) of 8.14x10⁻⁴ Pa-s. The free stream velocity was measured 5 turbine diameters upstream using an acoustic Doppler velocimeter (Nortek Vector) with a 32 Hz sampling rate. The free stream velocity (U_∞) was 0.91 m/s with a turbulence intensity of 2.9%. Here, we define the Reynold's number in terms of the blade chord and turbine diameter of 4.52x10⁴ and 1.9x10⁵, respectively for all experiments.

B. Turbine

A two-bladed (N=2) turbine was examined. The blades were NACA 0018 foils with a chord length, c, of 4.06 cm and a 6° preset pitch angle. The turbine was 17.2 cm in diameter, D, measured at the widest part of the blade (located at the quarter chord) and the blade span was 23.4 cm. To more readily image the mid-plane of the rotor with PIV, the end plates were oversized (40 cm diameter) acrylic. The turbine had a blockage ratio, β, of 11.6%, chord to radius ratio of 0.47 and a solidity, $\sigma = Nc/\pi D$, of 0.15.
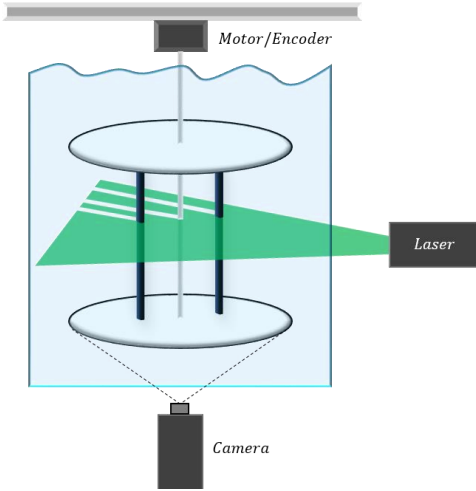
Fig. 3. Schematic of the experimental setup for taking the planar PIV data. The laser sheet is centered at the turbine mid-plane with the camera imaging from below. The turbine is mounting using a cantilever setup as to not obscure the field of view.

As shown in Fig. 1, the azimuthal position, θ, is defined such that $\theta = 0°$ corresponds to the turbine blade facing directly upstream. The nominal angle of attack, α_n, is defined as the angle between the foil chord line and the nominal incident velocity, U_n. The nominal velocity (relative velocity to the leading edge of the foil) is the vector sum of the tangential and free stream velocities. In the absence of any induced flow, its magnitude is

$$|U_n| = U_\infty \sqrt{\lambda^2 + 2\lambda \cos(\theta) + 1}. \quad (2)$$

The nominal angle of attack given at the leading edge is a function of the azimuthal position of the foil neglecting any turbine induction terms is

$$\alpha_n(\theta) = \tan^{-1}\left(\frac{\sin(\theta)}{\lambda + \cos(\theta)}\right) + \alpha_p \quad (3)$$

where α_p is the preset blade pitch angle. Here, the tip speed ratio and pitch angle are held constant for each test. A schematic of the blade geometry and graph of the nominal velocity and angle of attack over one turbine rotation are shown in Fig. 1 a-d for two tip-speed ratios of interest. The static stall angle, α_{ss}, for a NACA 0018 foil at a similar Reynold's number (Re_c=1.5x10^5) is 12.1° [9] and is plotted in Fig. 1d. for reference. We note that comparison between a rapidly-varying nominal angle of attack and steady-state stall angle can be misleading and should be considered only semi-quantitative.

C. Turbine Performance Measurement

The turbine was mounted on one end to a servomotor which was attached to a 6-axis load cell (ATI Mini45) and then to a rigid crossbeam above the free surface. The other end was connected to another 6-axis load cell (ATI Mini40) and then to a suction plate on the bottom of the flume, as shown in Fig 2. The turbine rotation was varied through 19 tip-speed ratios ranging from 1 to 2.8 in 0.1 increments. At each data point the tip-speed ratio was held constant and data was acquired for 60 seconds at 1 kHz. Turbine
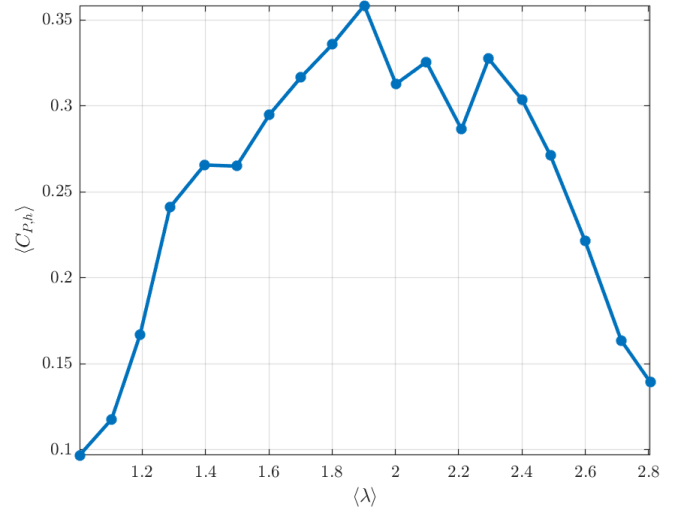

Fig. 4. Time average turbine performance, $C_{p,h}$ curve for λ between 1 and 2.8

position was extracted from the servomotor encoder with a resolution of 2^{18} counts/rotation.

Performance is characterized by the non-dimensional coefficient of performance ($C_{p,h}$) which is the ratio between the mechanical power produced by the turbine and the hydrodynamic power available in the flow,

$$C_{p,h} = \frac{\omega \tau_h}{\frac{1}{2}\rho U_\infty^3 2RL} \quad (4)$$

where τ_h is the hydrodynamic torque produced by the turbine, R is the turbine radius and L is the blade span (turbine height). Fig. 2 shows the turbine free body diagram for the experimental setup. Here τ_h is the hydrodynamic torque produced by the turbine, τ_c is the regulating control torque applied by the servomotor, and $\tau_{bearing}$ is the torque imparted on the turbine due to friction in the bearing. The top load cell measures $\tau_{m,top}$ to τ_c, and $\tau_{m,bottom}$ is the measured torque by the bottom load cell and is equal and opposite to $\tau_{bearing}$. For a constant angular velocity ($\dot\omega$=0) the equation of motion for the turbine becomes

$$\tau_h = -\tau_c - \tau_{bearing} = \tau_{m,top} + \tau_{m,bottom} \quad (5)$$

Turbine blade performance is calculated by subtracting the performance of the endplates alone from that of the full turbine assembly. It is important to note that this strategy will not capture any secondary interactions between the blades and the end plates, however, Strom et al. [10] found these effects to be negligible for a turbine similar to the one employed in the current study.

D. PIV Measurements

Two-dimensional, two-component, time-resolved velocity measurements were obtained at the center span of the blades in a streamwise plane parallel to the turbine

TABLE I
PARAMETERS FOR PIV INVESTIGATION

Image pairs per phase	75
Calibration	9.31 pix/mm
FoV	27.9 cm x 17.2 cm
Lens Focal Length	50 mm
Lens Aperture	f# = 16
Light sheet thickness	2 mm
Particle Image diameter	3 pixels
dt	0.5- 0.7 ms
Phase rotational separation	5-10 degrees

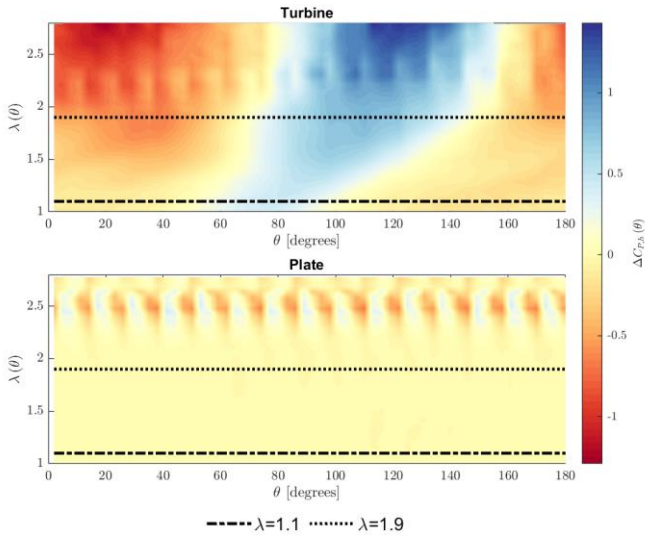Summary of the experimental parameters used in acquiring the planar PIV data.

Fig. 5. Difference in phase averaged and time averaged performance, $\Delta C_{p,h}$, plotted for all tip speed ratios and azimuthal positions for the two cases: turbine (top) and plates only (bottom). The two horizontal lines correspond to the chosen tip speeds λ=1.1 and 1.9.

endplates. The flow was illuminated using a dual cavity 30 mJ per pulse, Continuum Terra PIV Nd:YLF laser capable of a repetition rate of 10 kHz. The laser light sheet was approximately 2mm thick in the field of view (FoV). Images were captured with a Vision Research Phantom v641 high speed camera with 2560 x 1600 resolution resulting in a large field of view of 27.5 cm x 17.2 cm. The flow was seeded with 10 μm silver coated particles producing images of approximately 3 pixels in diameter. Other relevant PIV setup parameters are summarized in Table 1.

To maximize data yield in near-blade vortical regions, PIV exposure delay times, *dt*, were selected such that the freestream velocity displacement was approximately 5 pixels. A series of 17 image pairs were acquired per blade cycle, resulting in an angular displacement between frames of approximately 10 degrees. A total of 75 frames were acquired per phase, with the start of each set of 17 pairs triggered using a trigger from the turbine servomotor encoder. As a result, the phase averaged timing is highly accurate.

The blades were painted black to minimize laser reflections and maximize data yield in this area of interest. Remaining reflection was significantly mitigated through an average background subtraction of phase-matched
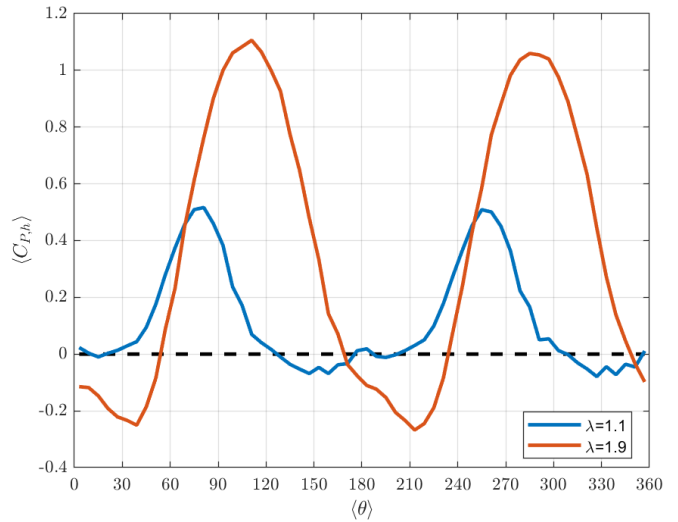

Fig. 6. Phase averaged coefficients of hydrodynamic performance, $C_{p,h}(\theta)$, plotted for both tip-speed ratios evaluated using PIV.

images. To obtain data adjacent to the suction and pressure sides of the turbine blades at all phases of interest, all PIV measurements were repeated with the turbine spinning in both clockwise and counter-clockwise directions. In this way, the influence of blade shadows on our resulting analysis is minimized. When conducting PIV measurements, the turbine was mounted in a cantilevered setup shown in Fig. 3 to ensure an unobstructed view of the near-blade flow field. Performance and PIV measurements could not be obtained concurrently because the cantilever moment would exceed the load cell rating.

Velocity fields were computed using a multi-pass, cross-correlation algorithm with iterative image deformation as implemented in TSI insight 11.1.0.5. A Gaussian mask was employed for each interrogation window. The window of the final pass was 32x32 pixels with a 50% overlap. Only vectors with a signal to noise ratio of 1.2 were accepted.

Vectors were validated using a normalized median filter with a 9x9 vector neighborhood and threshold of 2.5 [11]. Secondary correlation peaks were inserted when they satisfied this validation filter. Vorticity is calculated using a filtered second-order difference method as described by R. J. Adrian and J. Westerweel [12].

III. RESULTS AND DISCUSSION

E. Performance

Fig. 4 shows the time-averaged performance over the range of tip-speed ratios tested. The time-averaged data is used to determine an optimal and sub-optimal tip-speed ratios to investigate with planar PIV. The performance curve is not as smooth as would be expected for many cross-flow turbines, particularly for tip-speed ratios higher than observed for maximum performance (λ=1.9). Since the oppositional torque from the end plates exceeds the hydrodynamic torque produced by the blades at all tip-speeds, we believe that this is a consequence of either resonance in the end plates or resonance in the load cell.
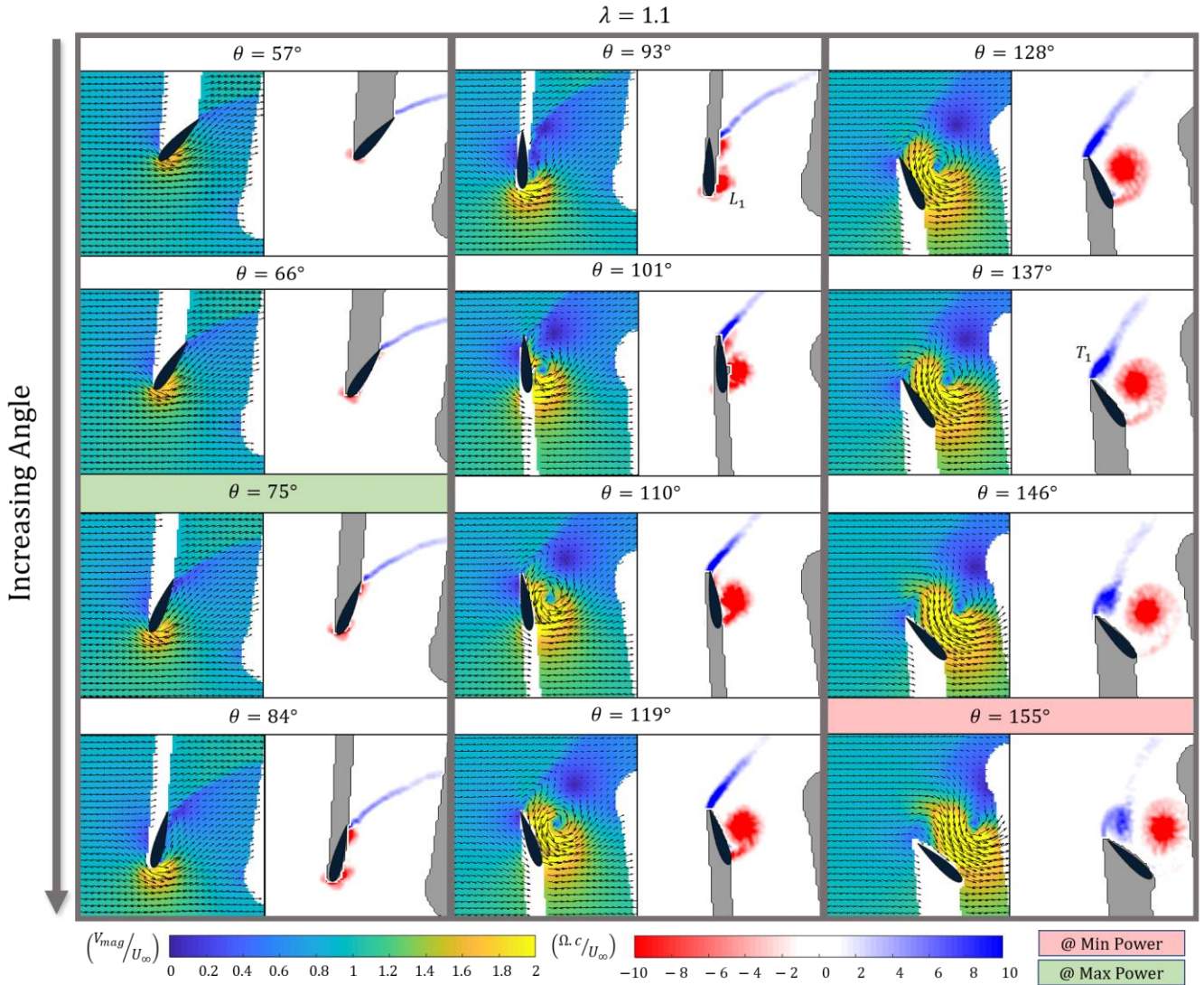
Fig. 7. Phase averaged velocity magnitude contour with every third vector plotted and vorticity contour for θ=57° to 155° for λ=1.1. L_1 and T_1 denote the LEV and TEV that form through the rotation. The phases corresponding to maximum and minimum $C_{p,h}$ are also indicated.

The difference between the time-averaged and phase-averaged performance values, $\Delta C_{p,h}$, are plotted in Fig. 5 for both the full turbine assembly and the plates only. Because the plate geometry is constant for all azimuthal positions, the performance should vary little with phase, meaning the difference between the phase-averaged and time-averaged values at each phase should be constant. This is seen for λ<2, but the "ringing" for $2 < \lambda < 2.5$ encompasses the jagged area on the $C_{p,h}(\lambda)$ curve in Fig. 4.

For this reason, the two tip-speed ratios chosen for PIV analysis (horizontal lines plotted in Fig. 5) are outside of this region and correspond to relatively poor (λ=1.1) and optimal performance (λ=1.9). The phase-average coefficient of power, $C_{p,h}(\theta)$, curves for these two cases are plotted in Fig. 6 a. The max $C_{p,h}$ for λ=1.1 is 0.5 and occurs at θ=165° and 345°. As in previous studies, $C_{p,h}$ for λ=1.9 exceeds unity at θ=90°-120° and again at θ=270°-300°. The phase shift in the peaks of the two $C_{p,h}(\theta)$ curves is due to the dependence of angle of attack on λ. The λ=1.1 case will surpass α_{ss} at an earlier phase than for λ=1.9 because it has a much higher maximum angle of attack. This means the λ=1.1 case has a higher probability of reaching deep dynamic stall and this may be contributing factor to the

significant reduction in performance as compared with λ=1.9. It is also interesting to note that while λ=1.9 has a higher maximum performance, it also has a larger and more defined minimum performance peak.

F. PIV

The PIV results for the upstream and downstream sweeps at λ=1.1 and 1.9 are shown below in Fig. 7-10. The phases of maximum and minimum power production ($C_{p,h}$) are indicated on each plot. For each phase, both a field of velocity magnitude with overlaid vector field (every third vector) and the vorticity are plotted. Red corresponds to clockwise rotation. All plots have been non-dimensionalized with the free stream velocity and the chord length. It is important to note both velocity shear and rotational motions contribute to vorticity. Initial examination reveals stronger induced velocities, vortex shedding, and blade/vortex interactions for λ=1.1 than for λ=1.9.

G. λ=1.1

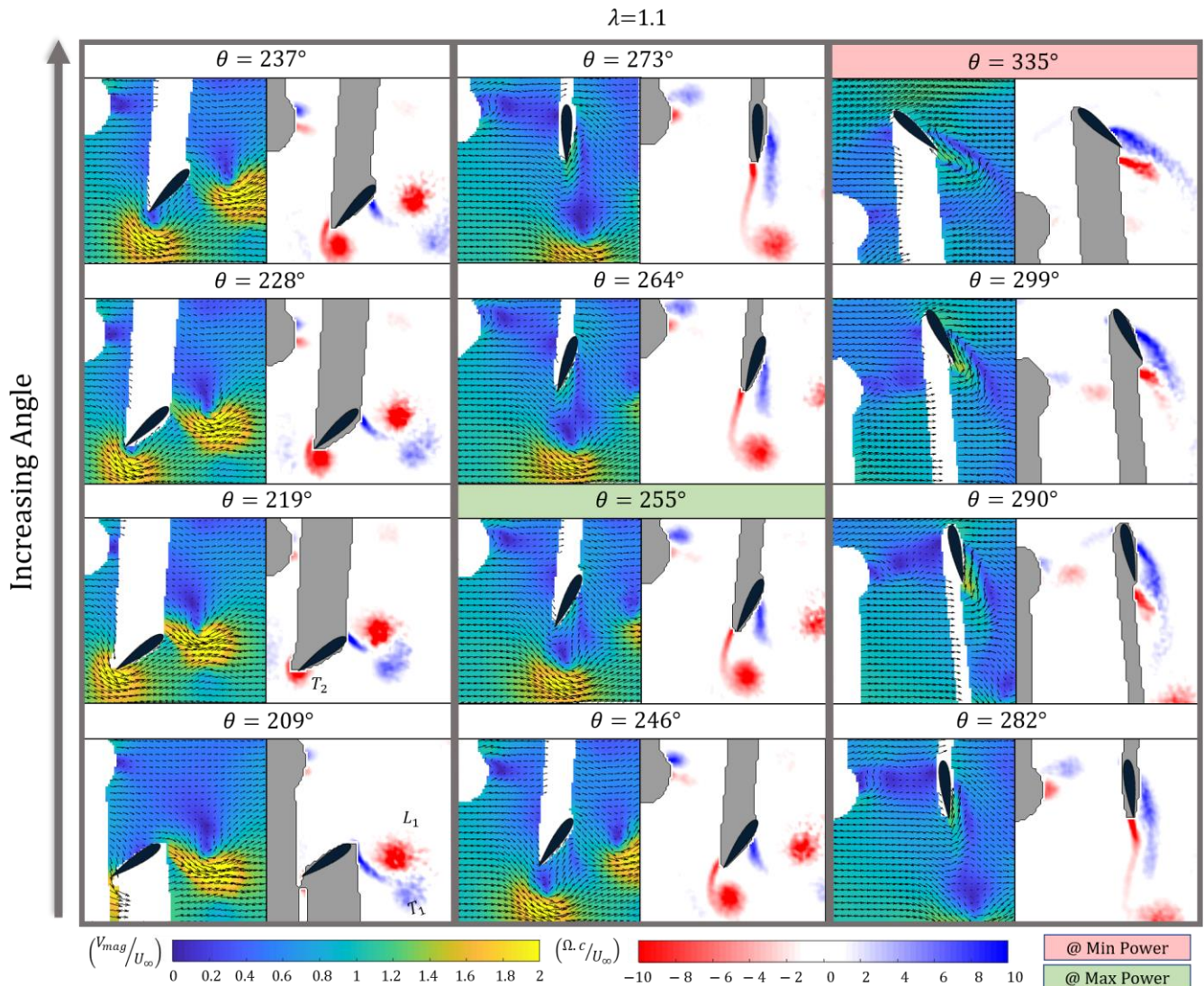Fig. 7 and 8 show the upstream and downstream near-blade flow fields at λ=1.1 for θ=57°-155° and θ=209°-335°

Fig. 8. Phase averaged velocity magnitude contour with every third vector plotted and vorticity contour for θ=209° to 335° for λ=1.1. L_1 are T_1 the vortices previously formed and shed during the upstream portion of the rotation and T_2 is the new TEV that forms at the beginning of the downstream rotation. The phases corresponding to maximum and minimum $C_{p,h}$ are also indicated.

respectively. Maximum power production occurs near θ =84° for the upstream blade and θ =264° for the downstream blade. At these positions a LEV, L_1, is forming on the upstream blade, indicating that it is entering dynamic stall and that lift on this blade is increasing beyond what is possible for a static blade. The downstream blade is seen to interact strongly with previously shed upstream vortices (L_1 and T_1), leading to counterflow on the downstream surface of the blade for all downstream phases shown in Fig 8. This strong stall is persistent and is a significant detriment to overall turbine performance. At the phase of maximum power, a new TEV (T_2) has formed on the downstream blade and has been shed into its wake, leaving the blade in a region of weak induced flow velocities. As a result, the downstream blade is producing less oppositional torque from drag at this position than at other phases. Interestingly, L_1 on the upstream blade continues to grow in strength and remain adjacent to the blade after the phase of maximum power is reached. This suggests that the performance of this blade continues to increase but is counter-acted by the oppositional torque on the downstream blade in this region during later phases.

Performance begins to decrease dramatically near θ = 93°, at which point the L_1 begins to detach and move away from the blade. This is consistent with the dramatic loss in lift observed on foils at the onset of deep dynamic stall. Minimum power production for this tip-speed ratio is a long trough from θ=120°-210° for the upstream blade and θ =300°-30° for the downstream blade. This region encompasses the detachment of the L_1 and the growth and strengthening of a TEV, T_1 on the upstream blade. The downstream blade remains stalled in this region, is exiting a lower velocity zone and is re-entering a zone closer to the free-stream velocity. There is thus a large contribution of drag opposing the direction of rotation and torque production. The absolute minimum occurs when the upstream blade is near θ= 155° and the downstream blade is near θ =335°. At this point the upstream blade has completely shed the L_1 and T_1 vortices.

Vortices from the previous rotation are not seen for λ=1.1. This is expected because the tangential velocity and the free stream and nearly equal, and therefore the vortices have more time to convect into the wake between rotations than for the λ=1.9 case.
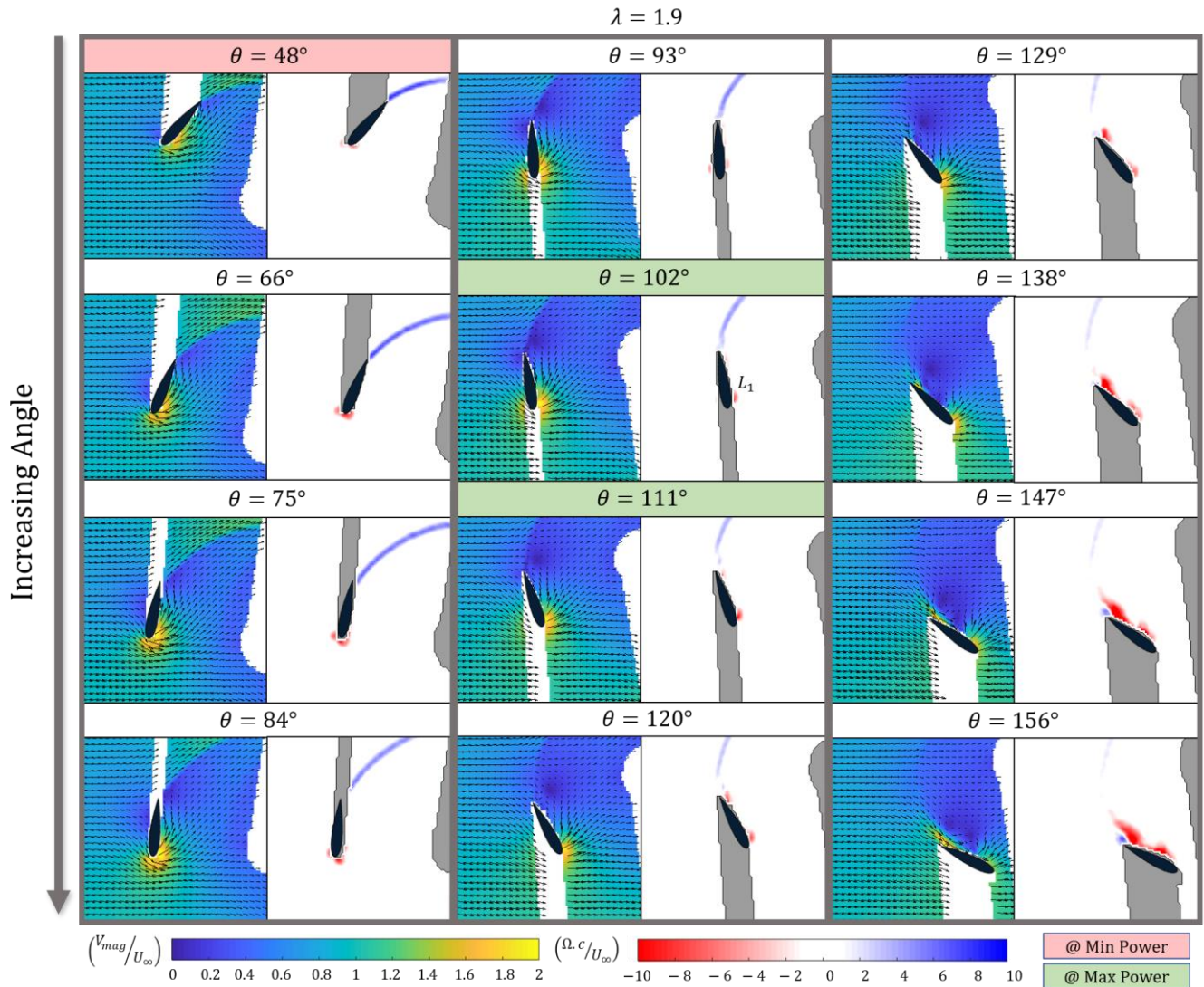
Fig. 9. Phase averaged velocity magnitude contour with every third vector plotted and vorticity contour for θ=57° to 156° for λ=1.9. L_1 denotes the LEV forming on the blade. The phases corresponding to maximum and minimum $C_{p,h}$ are also indicated.

H. λ=1.9

The maximum nominal angle of attack is much reduced for the λ=1.9 case (38° vs 71°) due to the higher blade speed. As a result, induced velocities are weaker, as are shed vortices. These vortices also tend to be tighter and smaller and were harder to capture with a vorticity metric due to a large contribution from velocity shear; a consequence of the higher blade speed. Fig. 9 and 10 show the upstream and downstream sweeps at λ=1.9 for θ=48°-156° and θ=209°-310° respectively. Maximum power production occurs when the upstream blade is between θ=102° and 111° and the downstream blade is between θ=292° and 282°. During this period the upstream blade appears to have a LEV, L_1 growing in strength with increasing phase and appears to not shed until past θ=156° however the large shear component in the vorticity makes the exact shedding angle difficult to determine. At the same time, the downstream blade is in a region of low velocity, with fully attached flow and no local vortex interaction and therefore may produce only a small amount of oppositional torque, likely leading to performance benefits. It is still unclear at this time why $C_{p,h} > 1$ is

observed at this phase but it may be due to the influence of L_1. Blockage may also be influencing this, however the normalised velocity incident to the blade is nowhere greater than one except near the tip of the blade where L_1 is and where the fluid would naturally move closer to the tangential velocity.

Performance begins a rapid decline when the upstream blade is near θ=129° at which point the L_1 vortex appears to begin to grow in size and travel towards the trailing edge. Minimum power production occurs for a narrower region than for the λ=1.1 case. It occurs near θ=48° for the upstream blade and near θ=209° for the downstream blade. Here, the upstream blade has a low α_n resulting in low forces and low lift while the downstream blade begins to completely shed the vortex, V_1. It is difficult to determine if this vortex originates as a LEV or TEV because of the high influence of shear in the upstream vorticity plots and the inability to image the actual shedding phase due to the blade shadow. Due to the location and strength it is speculated that this vortex originates as a LEV on the upstream blade. A second vortex, V_2, enters the frame at θ=237° and is shed between θ=156° and 209° however exact shedding phase was again not captured. The exact
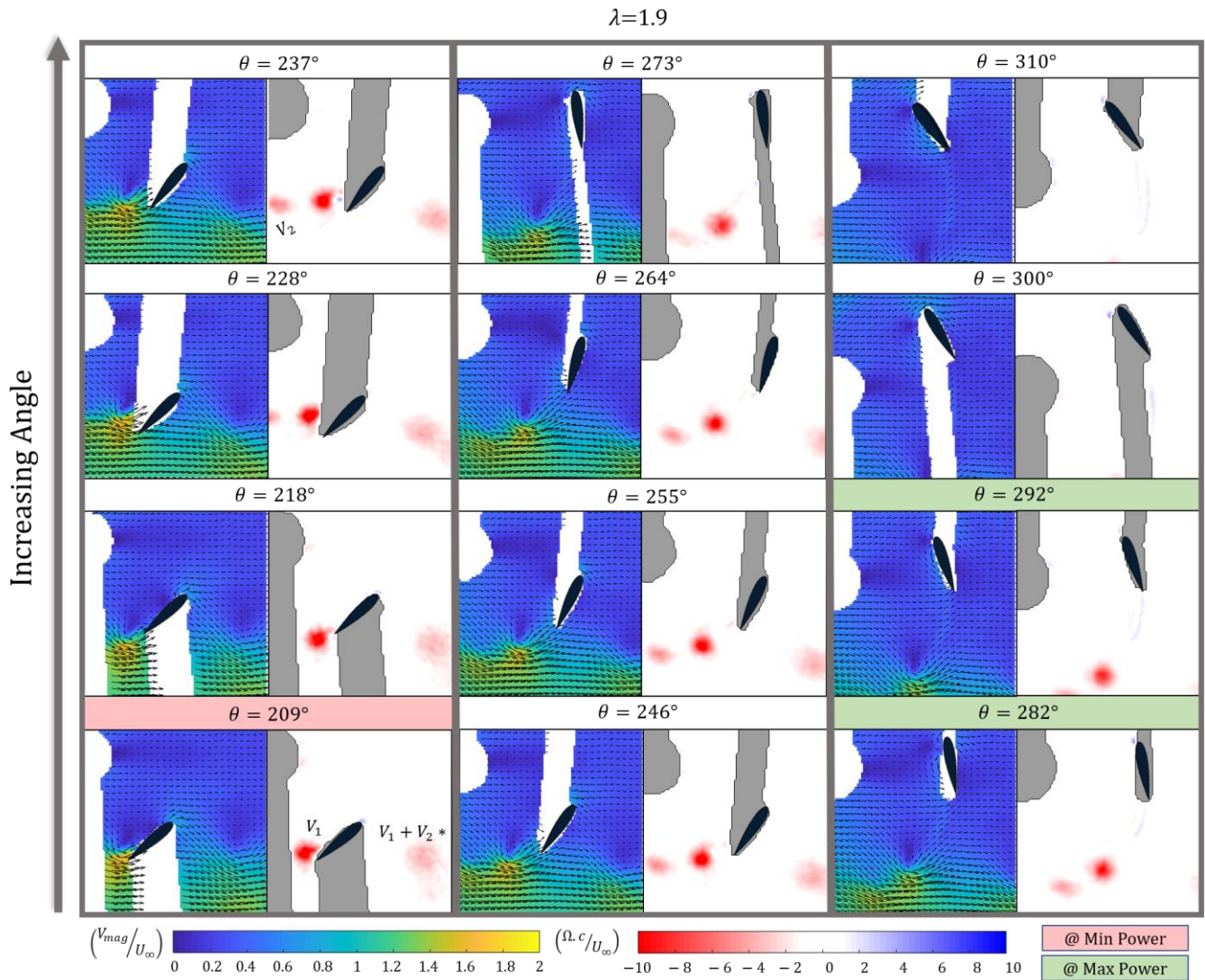
Fig. 10. Phase averaged velocity magnitude contour with every third vector plotted and vorticity contour for θ=209° to 310° for λ=1.9. V_1 and V_2 denote the vortices that previously formed and shed near the end of the upstream portion of the rotation. $V_1 + V_2 *$ denotes the combination of V_1 and V_2 that formed from the previous rotation.

formation and shedding location for these vortices may be unknown, however, it is clear that they are shed in quick succession which may explain the more pronounced minimum performance peak when compared to λ=1.1. Interestingly V_1 and V_2 are co-rotating and appear to eventually form a single vortex $V_1 + V_2$. The combination of these vortices remain in the FoV (denoted as $V_1 + V_2$ *) for the next rotation and may continue to influence the downstream blade there. Future examinations will use Q-criterion or swirling strength the isolate areas of pure rotation and better define the vortex shedding here.

I. Discussion

Significant differences exist between the in-rotor hydrodynamics of the λ=1.1 and λ=1.9 cases. At maximum power generation the upstream blade for both cases exhibits a strengthening LEV. This vortex is much more dramatic for the λ=1.1 case, however maximum power occurs before the LEV has reached maximum strength which is likely detrimental to turbine performance. The downstream blade for λ=1.1 almost always exhibits a strong counterflow on the downstream side, indicating

stall and a major loss of lift. The downstream blade for λ=1.1 continues to interact with shed vortices traveling close to the blade while for λ=1.9 the blade is in a low velocity region away from the influence of any shed vortices and the reversed flow is weaker. The differences between downstream blade flow fields may be cause for the increased performance for λ=1.9. Future work with a single-bladed turbine could further inform this hypothesis. The vortices that form for λ=1.9 are smaller and tighter than those formed for λ=1.1. This is likely attributed to the higher blade speed, smaller range in α_n and lower dynamic stall angle than for λ=1.1, all of which allow for a longer vortex attachment and growth time before shedding.

The flow on the downstream and upstream blades also varies significantly for the two cases at minimum performance. For λ=1.1 the upstream blade is in deep dynamic stall and downstream blade also continues to stall while entering a region of higher velocity as evident by the velocity profile. The upstream blade for λ=1.9 has $\alpha_n < \alpha_{ss}$ and smooth uniform flow. The downstream blade has just shed the second of two vortices and has the strongest

separated flow throughout the blade rotation. It appears these reasons contribute to λ =1.9 having a stronger minimum performance peak than λ=1.1.

Interestingly, the phase angle of flow separation for the current study appears delayed (between θ=156° and 209° for λ=1.9), when compared to previous studies. This is potentially due to the higher Reynold's number that is at least an order of magnitude higher than some previous studies. For comparison, in order of increasing Reynold's number:

1) Fujiwawa et al. [5] observed two pairs of stall vortices for λ=2; the first shedding between θ= 45° and 90° and the second between θ=90° and 135°.

2) Simão et al. [4] captured the convection of the LEV downstream by θ=108° for λ=2.

3) Somoano et al. [7] saw shedding at θ=135° for λ=1.7 and before θ=180° for λ=2.3.

4) Johnathan et al. [6] saw shedding between θ=80° and 100° for λ=2.

While some of this variation may be due to difficulties determining exact shedding phases and differences in turbine geometry, these results suggest that shedding phase may increase with Reynolds number. This is consistent with delayed separation caused by increased turbulence in the boundary layer at higher Reynold's number. Future experimentation is needed to confirm this hypothesis.

IV.   Conclusion

Through performance data measurement and 2D planar PIV, it has been shown that cross-flow turbine performance and the in-rotor hydrodynamics depend on tip-speed ratio and blade azimuthal position. In general, the coherent structures present in the low-performance case (λ =1.1) are more dramatic than for the high-performance case (λ =1.9). Both the upstream and downstream blades for λ=1.1 spend more time stalled than for λ=1.9 and have stronger interactions with vortices shed upstream. λ =1.9 has a larger, more pronounced performance peak than for λ=1.1, with the blades spending less of the rotation stalled and interacting little with previously shed vortices. Weaker induced velocities are present on the downstream blade and turbine induction has been shown to be higher for λ=1.9. This leads to less flow separation and weaker drag on this blade that consequently appears to have performance benefits. From these observations, the flow dynamics around the downstream blade between the two cases differ more than for the upstream blade. Further investigation is needed to determine if this has any performance implications. A brief comparison of our observations to prior experimental results shows that phase of vortex shedding may depend not only on tip speed ratio but possibly also on Reynolds number.

Potential future work includes, but is not limited to, isolating vortices from areas of strong shear with Q-criterion, swirling strength or similar, higher resolution PIV around shedding regions to better capture the dynamics, and experiments at a range of Reynolds number to investigate if/how shedding location changes.

References

[1] W. McCroskey, "The phenomenon of dynamic stall." National Aero- nautics and Space Administration Moffett Field CA, AMES Research Center, Tech. Rep., 1981.

[2] P. Ouro, T. Stoesser, and L. Ram, "Effect of Blade Cambering on Dynamic Stall in View of Designing Vertical Axis Turbines," vol. 140, no. June, pp. 1–12, 2018.

[3] T. Brunton, N. Jenkins, D. Sharpe, E. Bossanyi, "Aerodynamics of horizontal axis wind turbines," in *Wind Energy Handbook*, 2nd ed. Wiley, 2011, ch. *3*, sec. *A.3.5*, pp. *125*.

[4] C. Simão Ferreira, G. Van Kuik, G. Van Bussel, and F. Scarano, "Visualization by PIV of dynamic stall on a vertical axis wind turbine," *Exp. Fluids*, vol. 46, no. 1, pp. 97–108, 2009.

[5] N. Fujisawa and S. Shibuya, "Observations of dynamic stall on turbine blades," *J. Wind Eng. Ind. Aerodyn.*, vol. 89, no. 2, pp. 201–214, 2001.

[6] E. M. Jonathan, L. A. Danao, and R. J. Howell, "PIV measurements and CF simulation of the performance and flow physics and of a small-scale vertical axis wind turbine," *Wind Energy*, vol. 18, pp. 201–217, 2015.

[7] M. Somoano and F. J. Huera-Huarte, "Flow dynamics inside the rotor of a three straight bladed cross-flow turbine," *Appl. Ocean Res.*, vol. 69, pp. 138–147, 2017.

[8] Polagye, B., Strom, B., Ross, H., Forbush, D., and Cavagnaro, R., "Comparison of cross-flow turbine performance under torque-Regulated and speed-regulated control," Submitted to: *Journal of Renewable and Sustainable Energy*.

[9] W. A. Timmer, "Two-Dimensional Low-Reynolds Number Wind Tunnel Results for Airfoil NACA 0018," *Wind Eng.*, vol. 32, no. 6, pp. 525–537, 2008.

[10] B. Strom, N. Johnson, and B. Polagye, "Impact of blade mounting structures on cross-flow turbine performance," *J. Renew. Sustain. Energy*, vol. 10, no. 3, pp. 1–12, 2018.

[11] J. Westerweel and F. Scarano, "Universal outlier detection for PIV data," *Exp. Fluids*, vol. 39, no. 6, pp. 1096–1100, 2005.

[12] R. J. Adrian and J. Westerweel, "Postprocessing," in *Particle Image Velocimetry*, Cambridge, 2011, ch. *9*, sec. 9.3, pp. *432-433*